RAA 2019 Vol. **19** No. **12**, 179(12pp) doi: 10.1088/1674–4527/19/12/179

http://www.raa-journal.org *http://iopscience.iop.org/raa*

***R**esearch in*
***A**stronomy and*
***A**strophysics*

The jet of FSRQ PKS 1229−02 and its misidentification as a γ-ray AGN

Wei Zhao[1,2], Xiao-Yu Hong[1,2,3,4], Tao An[1,2] and Jun Yang[5]

[1] Shanghai Astronomical Observatory, Chinese Academy of Sciences, Shanghai 200030, China; *weizhao@shao.ac.cn*
[2] Key Laboratory of Radio Astronomy, Chinese Academy of Sciences, Nanjing 210008, China
[3] University of Chinese Academy of Sciences, Beijing 100049, China
[4] Shanghai Tech University, Shanghai 201210, China
[5] Department of Earth and Space Sciences, Chalmers University of Technology, Onsala Space Observatory, SE-439 92 Onsala, Sweden

Received 2019 April 27; accepted 2019 July 4

Abstract Flat-spectrum radio quasar PKS 1229−02 with a knotty and asymmetric radio morphology was identified as the optical and radio counterpart of a γ-ray source. In this paper, we study the properties (e.g. morphology, opacity, polarization and kinematics) of the jet in PKS 1229−02 using radio interferometry. With our results, we find that the knotty and asymmetric morphology of this source may probably shaped by the interaction between its anterograde jet and the nonuniform dense ambient medium. By reproducing a Spectral Energy Distribution of PKS 1229−02 with the obtained kinematic parameters, we find that the relativistic beaming effect in PKS 1229−02 is not strong enough to produce the reported γ-ray emission, i.e. PKS 1229−02 may not be a γ-ray AGN. The misidentification may probably be due to the poor spatial resolution of the γ-ray detector of the previous generation.

Key words: galaxies: individual (PKS 1229−02) — galaxies: jets — radio continuum: galaxies

1 INTRODUCTION

Flat-spectrum radio quasar (FSRQ) PKS 1229−02 shows an asymmetric "core-jet-lobe" kpc-scale radio morphology. As shown in Kronberg et al. (1992), the radio emission extends for about 15 arcseconds towards northeast of the most luminous region (since this region has been identified as core by Kronberg et al. 1992, which will be referred as "core" hereafter), while it extends for only about 5 arcseconds towards the southwest. The southwest jet often seems to be deflected as propagating outward: as shown by the 5 and 15 GHz VLA maps in Kronberg et al. (1992), first it is deflected northward within 1 arcsecond from the core; further, at about 2 arcseconds from the core, it is deflected southward and finally joints the southwest lobe. The southwest kpc-scale jet is very knotty. It was also detected in the X-ray band (Tavecchio et al. 2007), while some of its knots were also detected in the optical band (Le Brun et al. 1997).

PKS 1229−02 was identified as the optical and radio counterpart of an EGRET-detected γ-ray source 3EG J1230–0247 (Thompson et al. 1995; Hartman et al. 1999), which is positionally associated with a Fermi-detected γ-ray source 3FGL J1228.4–0317 (Abdo et al. 2009). γ-ray sources are often identified as active galactic nuclei (AGNs) with extremely relativistic jets aligned to our line of sight, e.g. FSRQ and BL lacs. Relativistic time dilation, Doppler boosting, together with projection effect, often bring about violent variations of luminosity, extremely high observed brightness temperature, and compact source structure in these γ-ray AGNs. In most theories propounded to explain the γ-ray emission from AGNs, relativistic beaming is always considered as a crucial role, no matter whether the emission particles are leptons (Böttcher 2000; Marscher & Gear 1985; Maraschi et al. 1992; Bloom & Marscher 1996; Dermer & Schlickeiser 1993; Arbeiter et al. 2002; Dondi & Ghisellini 1995) or hadrons (Rachen 2000; Protheroe 1997; Mücke & Protheroe 2001) in these theories. But PKS 1229−02 only shows a very low optical variability (Wills et al. 1992; Raiteri et al. 1998; Romero et al. 2002) which is quite unusual for a γ-ray AGN, and whether there is extremely high observed brightness tem-

perature or not, or whether its structure is compact or not, are still unknown.

In this paper, we study the properties of the jet in PKS 1229−02, including the morphology, opacity, polarization, and kinematics. With the obtained results, we investigate the interaction between the jet and the surrounding medium, we then reproduce a Spectral Energy Distribution (SED) for PKS 1229−02 with the obtained kinematic parameters, and discuss the possibility for PKS 1229-02 as a γ-ray AGN (or not). We use these cosmological parameters throughout this paper: $H_0 = 71$ km s^{-1} Mpc^{-1}, $\Omega_M = 0.27$, $\Omega_\Lambda = 0.73$. At the distance of PKS 1229−02($z = 1.045$), 1 mas corresponds to 8.126 pc, and 1 mas yr^{-1} corresponds to 28.5 c (Wright 2006).

2 OBSERVATIONS AND DATA REDUCTION

From 1997 to 2002, we conducted a series of observations with Very Large Array (VLA), European VLBI Network (EVN), and Very Long Baseline Array (VLBA) to make studies on a sample of γ-ray AGNs with radio counterparts, among which, PKS 1229−02 was observed in five tracks, including one track using VLA C-array at 8.5 and 22.5 GHz, one track using VLA A-array at 8.5 and 22.5 GHz, one EVN track at 5.0 GHz, one VLBA track at 1.6 GHz, and another VLBA track at 4.9, 8.4 and 15.0 GHz. All the VLA and VLBA tracks were conducted in dual circular-polarization mode while the EVN track was in left circular-polarization mode. The VLA and VLBA data are recorded in 2-bit format with a total bandwidth of 50 and 64 MHz respectively and correlated in Socorro, New Mexico, USA, while the EVN data were recorded in 2-bit format with a bandwidth of 28 MHz and correlated in Bonn, Germany. In additional, we acquired two sets of open-accessed 8.4 GHz VLBA data to study the kinematics of pc-scale jet of PKS 1229−02. Details of the observations are listed in Table 1.

We performed the initial calibration with the AIPS (Astronomical Image Processing System) software package (Diamond 1995) following the standard procedures of VLA and VLBI data reduction. For VLBA tracks, we performed several certain steps to calibrate the polarization: we determined and removed the variations of the parallactic angles with a procedure VLBAPANG; we determined the R-L delay difference with another procedure VLBACPOL on a highly polarized source (e.g. DA193, 3C 279); we calibrated the instrumental polarization with AIPS task LPCAL by using scans on a radio source with a compact structure (e.g. DA193, OQ 208); and, the absolute polarization angle was corrected by comparing the apparent Electric Vector Position Angle (EVPA) of calibrators with the quasi-simultaneous measurements in the VLA/VLBA Polarization Calibration Page[1]. After initial calibration, we split the data into single-source files and imported them into the Caltech VLBI Program DIFMAP (Shepherd et al. 1994) for self-calibration and imaging. We performed self-calibration/Imaging loops for multiple iterations to obtain images with high dynamical ranges. The parameters of the images, e.g. beam size, peak intensity, and root-mean-square noise (σ) are listed in Tables 2 and 3.

3 RESULTS

3.1 Structure of the Jet

We present the VLA and VLBI maps of PKS 1229−02 in Figures 1 and 2 respectively (see details of the maps in Tables 2 and 3). As our VLA maps show, the kpc-scale morphology of PKS 1229−02 is quite consistent with that in Kronberg et al. (1992). As our VLBI maps show, the pc-scale jet in PKS 1220−02 aligns well with the innermost part of the kpc-scale southwest jet in PKS 1220−02, suggesting that the southwest jet goes toward our line of sight (referred as "the anterograde jet" hereafter), while its northeast counterpart goes against our line of sight (referred as "the retrograde jet" hereafter). The pc-scale jet is as knotty as its kpc-scale counterpart, but shows no significant curvature on the maps.

To further analyze the properties of the jet in PKS 1229−02, we fitted the $u-v$ data as Gaussian components with procedure MODELFIT in DIFMAP. The most luminous regions of the source on both kpc- and pc-scales are often fitted with elliptical Gaussians, while the rest part of the source is often fitted with circular Gaussians. The uncertainties of the fitted parameters are estimated as in Fomalont et al. (2004) and Lee et al. (2008). The fitted values are listed in Tables 2 and 3. The locations of the fitted Gaussians are indicated in Figures 1 and 2.

On the kpc-scale, the core component which has already been identified by Kronberg et al. (1992) is renamed as $\mathrm{C_{VLA}}$, which is the only detected component on VLA A-array map at 22.5 GHz. The retrograde lobe and jet are clearly detected on VLA C-array map at 8.5 GHz, and could be fitted with two Gaussian components named as E1 and E2 respectively. But E2 is undetected on the maps

[1] `http://www.vla.nrao.edu/astro/calib/polar`

Table 1 Observations

Obs.Code	Array	Telescope [a]	Epoch	Frequency (GHz)	Bandwidth (MHz)	Correlator
(1)	(2)	(3)	(4)	(5)	(6)	(7)
VLA						
AH635	VLA-C	full array	1999.06	8.5, 22.5	50	VLA
AH721	VLA-A	full array	2000.92	8.5, 22.5	50	VLA
VLBI						
EH003	EVN	Ef Sh Jb Mc Nt Ht On Wb Ur Tr	1997.85	C	28	MK III [b]
BH065	VLBA	full array	2000.15	1.6	64	VLBA [c]
BH096	VLBA	full array	2002.55	4.9, 8.4, 15.0	64	VLBA [c]
archived VLBI data						
BB023	VLBA	full array	1997.35	8.4	32	VLBA[c]
BL170	VLBA	BR FD HN KP LA MK NL OV SC	2010.51	8.4	64	VLBA[c]

Note: [a] The telescopes with strong fringes: Ef: Effelsberg; Sh: Shanghai; Jb: Jodrell Bank; Mc: Medicina; Nt: Noto; On: Onsala; Hh: Hartebeesthoek; Sm: Simiez; Ur: Urumqi; Wb: WSRT; Tr: Torun; BR: Brewster; FD: Fort Davis; HN: Hancock; KP: Kitt Peak; LA: Los Alamos; MK: Mauna Kea; NL: North Liberty; OV: Owens Valley; SC: St. Croix; [b] The MK III correlator at MPIfR (Bonn, Germany); [c] The VLBA correlator at NRAO (Socorro, USA).

Table 2 VLA Images

Epoch (yr)	Array	Frequency (GHz)	Beam Size [a] (arcsec×arcsec, degree)	$I_{\rm peak}$ [b] (Jy beam^{-1})	1σ [c] (mJy beam^{-1})	Contour [d] (mJy beam^{-1})
(1)	(2)	(3)	(4)	(5)	(6)	(7)
1999.06	VLA-C	8.5	3.22×2.34, 13.9	0.75	0.06	$0.25 \times (-1, 1, 2, 4, ..., 2048)$
		22.5	1.35×0.96, 17.4	0.51	0.17	$0.66 \times (-1, 1, 2, 4, ..., 512)$
2000.92	VLA-A	8.5	0.39×0.25, 37.8	0.47	0.11	$0.45 \times (-1, 1, 2, 4, ..., 1024)$
		22.5	0.17×0.12, 36.5	0.15	0.22	$0.86 \times (-1, 1, 2, 4, ..., 128)$

Notes: [a] The restoring beam FWHM size of the CLEANed images; [b] The peak flux density on the CLEANed images; [c] The root-mean-square noise of the CLEANed images; [d] The levels of the contours of the CLEANed images.

Table 3 VLBI Images

Epoch (yr)	Array	Frequency (GHz)	Beam Size [a] (mas×mas, degree)	$I_{\rm peak}$ [b] (Jy beam^{-1})	1σ [c] (mJy beam^{-1})	Contour [d] (mJy beam^{-1})
(1)	(2)	(3)	(4)	(5)	(6)	
1997.85	EVN	5	1.88×1.36, 37.7	0.30	0.21	$0.63 \times (-1, 1, 2, 4, ..., 256)$
2000.15	VLBA	1.6	11.10×4.94, –1.6	0.34	0.22	$0.66 \times (-1, 1, 2, 4, ..., 512)$
2002.55	VLBA	4.9	3.71×1.69, –1.1	0.34	0.12	$0.36 \times (-1, 1, 2, 4, ..., 512)$
		8.4	2.24×1.04, –0.0	0.32	0.14	$0.42 \times (-1, 1, 2, 4, ..., 512)$
		15.0	1.33×0.57, –5.0	0.29	0.29	$0.87 \times (-1, 1, 2, 4, ..., 256)$

Notes: [a] The restoring beam FWHM size of the CLEANed images; [b] The peak flux density on the CLEANed images; [c] The root-mean-square noise of the CLEANed images; [d] The levels of the contours of the CLEANed images.

of VLA C-array at 22.5 GHz and VLA A-array at 8.5 GHz. The knotty morphology of the anterograde jet is best revealed by VLA A-array map at 8.5 GHz. This could be fitted with five Gaussian components named W1 to W5, from the edge to the center of the source, in which W3, W4, and W5 may correspond to the radio counterparts of the optical knots detected by HST (Le Brun et al. 1997). On the maps of VLA C-array, for the lower angular resolution, W5 could not be resolved from the core. Neither W2, W3, and W4 could be resolved from each other, so we fit them as a Gaussian component named as W2-W4.

On the kpc-scale, the asymmetric structure of PKS 1229−02 is clearly revealed by our results, as the integral flux density of the anterograde jet is a few times higher than that of the retrograde jet. The source is edge-brightened on kpc-scale, i.e. the jet components at the far-end of the source (e.g. W1, W2, E1) tend to have higher integral flux density than the jet components at the middle of the source (e.g. W3, W4, W5, E2).

On the pc-scale, the most luminous component is fitted with a Gaussian named as C (referred as "VLBI core" hereafter), while the rest part of the source is fitted with five Gaussian components named as A1 to A5 from the edge to the center (A5 could not be resolved from the VLBI core by the observations under 8.4 GHz). These components align well with each other in a line with a position

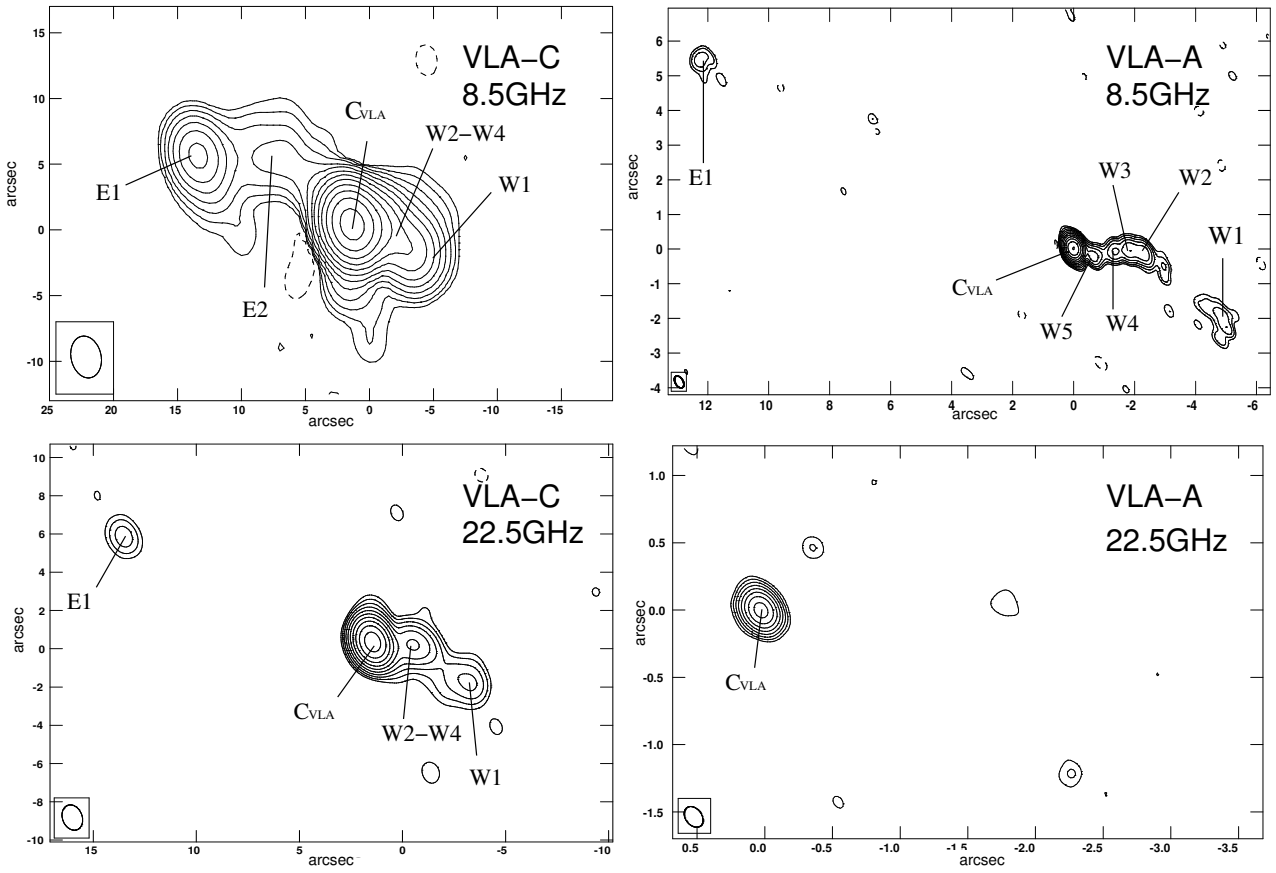

Fig. 1 VLA maps showing the kpc-scale morphology of PKS 1229−02. The locations of the fitted Gaussians $\mathrm{C_{VLA}}$, W5, W4, W3, W2, W1, E2, and E1 are indicated on the maps.

angle (PA) of -113° to the north, so we use the line with $PA \sim -113^\circ$ to the north as the approximate jet axis in the following analysis.

To make it clear if PKS 1229−02 is affected by major Doppler boosting or not, we estimate the brightness temperature T_b for the pc-scale components in the parent-galaxy rest frame with the method in Guijosa & Daly (1996).

$$T_\mathrm{b} = 1.77 \times 10^{12}(1+z)\frac{S_\mathrm{ob}}{\nu_\mathrm{ob}^2\theta_d^2}\mathrm{K} \qquad (1)$$

in which S_ob is the flux density in Jy, ν_ob is the observing frequency in GHz, and θ_d is the angular size of a Gaussian component in mas. In this paper, $\theta_d = \sqrt{ab}$, in which, a and b are the length of the major and minor axis of a Gaussian component respectively. The estimated values of T_b are listed in the last column of Table 5. We compare T_b of the VLBI core with T_eq, the brightness temperature of a radio source in the equipartition between the energy of the radiating particles and the magnetic field, which is often used as an upper limit of the intrinsic brightness temperature. As equation (4a) in Readhead (1994),

$$T_\mathrm{eq} = 1.6 \times 10^{12} h^{-2/17} F(\alpha)^{-2} \left\{\frac{1-(1+z)^{-1/2}}{1+z}\right\}^{2/17} \times (1+z)^{(2\alpha-13)/17} S_\mathrm{op}^{1/17} (\nu_\mathrm{op} \times 10^3)^{(1-2\alpha)/17}\mathrm{K} \qquad (2)$$

in which α is the spectral index with a typical value of -0.75, and $F(\alpha)$ is a factor with a typical value of 3.4, then $T_\mathrm{eq} \sim 0.5 \times 10^{11}$K. As we see, T_b of the VLBI core is at the order of magnitude of 10^{10}K or 10^{11}K, almost the same as the T_eq, suggesting that PKS 1229−02 is not affected by major Doppler boosting.

On both kpc and pc-scale, the structure of PKS 1229−02 could not be described as "very compact". For example, on the kpc-scale, at 8.5 GHz, the integral flux density of $\mathrm{C_{VLA}}$ is 0.76 and 0.63 Jy on the maps of VLA C-array and A-array respectively, which means almost 20% of its flux density is resolved by the longer baselines of the VLA-A array. Moreover, on pc-scale, the VLBI core takes only 52% to 64.1% of the total integral flux density of the source.

Table 4 Kpc-scale Jet Components

Epoch (yr) (1)	Array (2)	Frequency (GHz) (3)	Comp. (4)	S_c [a] (mJy) (5)	r [b] (arcsec) (6)	PA [c] (degree) (7)	a [d] (arcsec) (8)	a/b [e] (9)	Φ [f] (degree) (10)
1999.06	VLA-C	8.5	C_{VLA}	764±27	0	–	0.45±0.01	0.5	50.2
			W2-W4	74±10	2.12±0.01	–90.1±0.3	0.42±0.02	1.0	
			W1	40±6	4.87±0.09	–112.0±1.0	1.48±0.17	1.0	
			E2	13±6	7.80±1.14	46.8±8.4	5.04±2.28	1.0	
			E1	24±5	13.09±0.08	66.3±0.4	1.10±0.17	1.0	
		22.5	C_{VLA}	530±30	0	–	196.0±7.2	0.58	27.4
			W2-W4	42±8	1.94±0.08	–94.5±2.4	0.95±0.17	1.0	
			W1	18±6	4.91±0.23	–114.5±2.7	1.41±0.46	1.0	
			E1	5±3	13.34±0.12	65.2±0.6	0.57±0.26	1.0	
2000.92	VLA-A	8.5	C_{VLA}	630±40	0	–	214.5±9.8	0.4	–41.3
			W5	19±7	0.71±0.04	–107.9±2.8	0.24±0.07	0.85	–67.6
			W4	16±6	1.36±0.06	–93.6±2.4	0.33±0.12	0.29	–56.8
			W3	21±7	1.82±0.04	–91.4±1.1	0.27±0.07	0.63	–21.0
			W2	33±10	2.27±0.06	–93.2±1.6	0.45±0.12	0.62	66.9
			W1	31±25	4.98±0.75	–112.1±8.7	1.901±1.50	0.38	61.6
			E1	12± 8	13.32±0.17	65.9±0.7	0.56±0.35	0.58	–68.6
		22.5	C_{VLA}	180±20	0	–	0.07±0.01	0.76	–27.3

Notes: [a] The integral flux density; [b] The distance to the "core" component; [c] The position angle to the "core" component; [d] The length of the major axis; [e] The ratio between the length of the major and minor axis; [f] The position angle of the major axis.

Table 5 Pc-scale Jet Components

Epoch (yr) (1)	Array (2)	Frequency (GHz) (3)	Comp. (4)	S_c [a] (mJy) (5)	r [b] (mas) (6)	PA [c] (degree) (7)	a [d] (mas) (8)	a/b [e] (9)	Φ [f] (degree) (10)	T_b [g] (K) (11)
1997.35	VLBA	8.4	C	429±32	0	–	0.41±0.02	1.00	–	1.28×10^{11}
			A5	112±18	0.76±0.02	–109.1±1.5	0.46±0.04	1.00	–	2.72×10^{10}
			A4	39±14	2.96±0.36	–110.8±7.2	2.17±0.72	1.00	–	4.25×10^{8}
			A3	72±18	7.06±0.24	–115.4±2.0	1.97±0.48	1.00	–	9.55×10^{8}
			A2	77±17	10.25±0.15	–109.4±0.9	1.55±0.31	1.00	–	1.65×10^{9}
1997.85	EVN	5.0	C	366±30	0	–	1.05±0.07	0.40	66.0	1.20×10^{11}
			A4	45±17	3.09±0.48	–118.0±8.9	2.69±0.96	1.00	–	9.09×10^{8}
			A3	73±15	7.48±0.13	–116.2±1.0	1.34±0.26	1.00	–	5.86×10^{9}
			A2	88±19	10.17±0.24	–109.4±1.4	2.27±0.48	1.00	–	2.46×10^{9}
2000.15	VLBA	1.6	C	387±24	0	–	3.11±0.14	0.49	76.8	1.15×10^{11}
			A	216±19	7.35±0.24	–110.9±1.9	6.82±0.48	0.10	74.3	6.58×10^{10}
			A1	8±4	33.90±2.71	–112.2±4.6	12.32±5.43	0.44	–3.1	1.66×10^{8}
2002.55	VLBA	4.9	C	397±27	0	–	1.01±0.05	1.00	–	0.59×10^{11}
			A4	65±11	2.93±0.16	–115.0±3.1	2.22±0.32	1.00	–	1.98×10^{9}
			A3	83±12	7.29±0.14	–115.1±1.1	2.08±0.28	1.00	–	2.89×10^{9}
			A2	131±16	10.35±0.12	–110.9±0.6	2.18±0.23	1.00	–	4.19×10^{9}
		8.4	C	344±24	0	–	0.66±0.03	0.30	77.0	1.35×10^{11}
			A5	101±14	0.86±0.01	–101.1±0.9	0.42±0.02	1.00	–	2.94×10^{10}
			A4	56±12	3.15±0.26	–115.3±4.8	2.70±0.53	1.00	–	3.91×10^{8}
			A3	65±13	7.84±0.21	–115.2±1.5	2.20±0.42	1.00	–	6.84×10^{8}
			A2	91±14	10.69±0.13	–110.4±0.7	1.83±0.27	1.00	–	1.40×10^{9}
		15.0	C	340±24	0	–	0.33±0.02	0.64	80.4	0.78×10^{11}
			A5	124±15	0.88±0.02	–102.8±1.4	0.43±0.04	1.00	–	1.08×10^{10}
			A4	35±12	3.52±0.30	–109.5±4.9	1.82±0.61	1.00	–	1.68×10^{8}
			A3	44±15	7.89±0.31	–115.3±2.3	1.88±0.62	1.00	–	2.00×10^{8}
			A2	65±16	10.85±0.20	–110.3±1.1	1.66±0.40	1.00	–	3.77×10^{8}
2010.51	VLBA	8.4	C	410±32	0		0.35±0.02	0.83	1.68	2.03×10^{11}
			A5	48±11	1.05±0.05	–98.7±2.6	0.63±0.10	1.00	–	6.11×10^{9}
			A4	59±21	3.46±0.57	–112.8±9.5	3.37±1.15	1.00	–	2.68×10^{8}
			A3	58±20	8.85±0.42	–114.5±2.7	2.54±0.85	1.00	–	4.61×10^{8}
			A2	82±20	11.52±0.23	–110.4±1.2	2.00±0.47	1.00	–	1.05×10^{9}

Note: [a] The integral flux density; [b] The distance to the core component; [c] The position angle to the "core" component; [d] The length of major axis; [e] The ratio between the length of the major and minor axis; [f] The position angle of the major axis; [g] The brightness temperature.

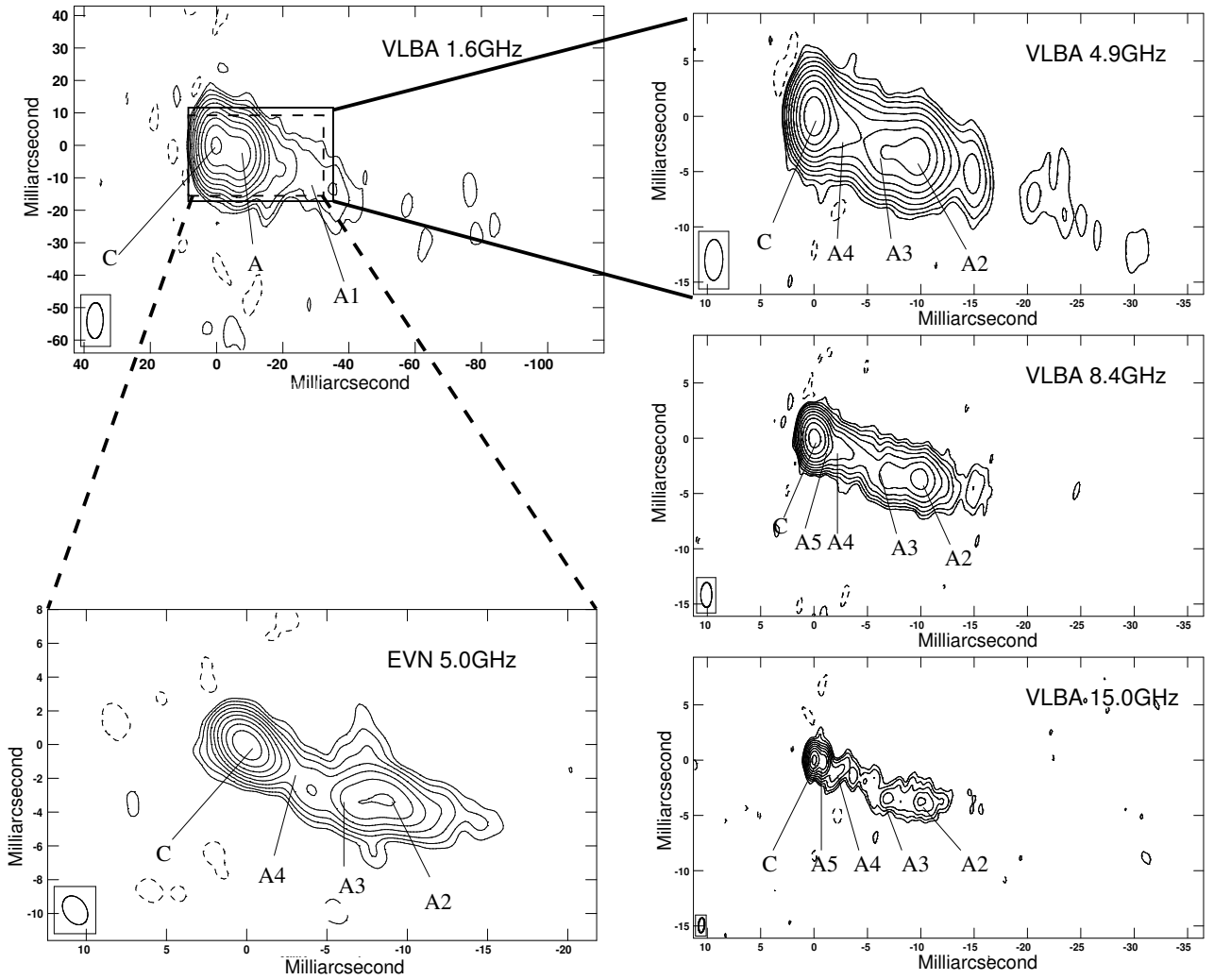

Fig. 2 VLBI maps showing the pc-scale morphology of PKS 1229−02. The locations of the fitted Gaussians C, A5, A4, A3, A2 and A1 are indicated on the maps.

3.2 Opacity of the Jet

To study the opacity of the kpc-scale jet in PKS 1229−02, we estimate the spectral index α of each jet components with the integral flux density fitted with VLA C-array data at 8.5 and 22.5 GHz, in the context of $S_{\rm obs} \propto \nu_{\rm obs}^{\alpha}$, in which $S_{\rm obs}$ is the observed integral flux density, and $\nu_{\rm obs}$ is the observing frequency. For the core component $\rm C_{VLA}$, $\alpha = -0.4$. For W2-W4 and W1, $\alpha = -0.6$ and -0.8 respectively. The flat spectrum of the anterograde jet suggests substantial low-frequency absorption, probably brought by the dense ambient medium. This is consistent with what was inferred by Kronberg et al. (1992)—the anterograde jet interacts with the external environment as propagating outward. For component E2, $\alpha = -1.6$. Although E1 is not detected at 22.5 GHz, if we use 3σ of the 22.5 GHz map as the upper limit of its peak intensity, then the upper limit of α is -2.9. So the retrograde jet has an optical thin spectrum.

To study the opacity of the pc-scale jet in PKS 1229−02, we produce two spectral index maps with the data of the multi-frequency VLBA track conducted in the epoch of 2002.55. We first image the fully self-calibrated data of two adjacent frequencies (i.e. 4.9 and 8.4 GHz, 8.4 and 15.0 GHz) in the same $u - v$ range, then restore the resulting images with the same synthesized beam, and finally combine two images by aligning their map centers. The maps showing distribution of spectral index with pseudo-color are superimposed on the intensity contour plots of 4.9 and 8.4 GHz VLBA maps, respectively, and presented in the upper and middle panels of Figure 3, respectively. The color is only shown where the intensity is above 3σ. We find that the inverted spectrum with $\alpha > 0$ is detected in the vicinity of the VLBI core

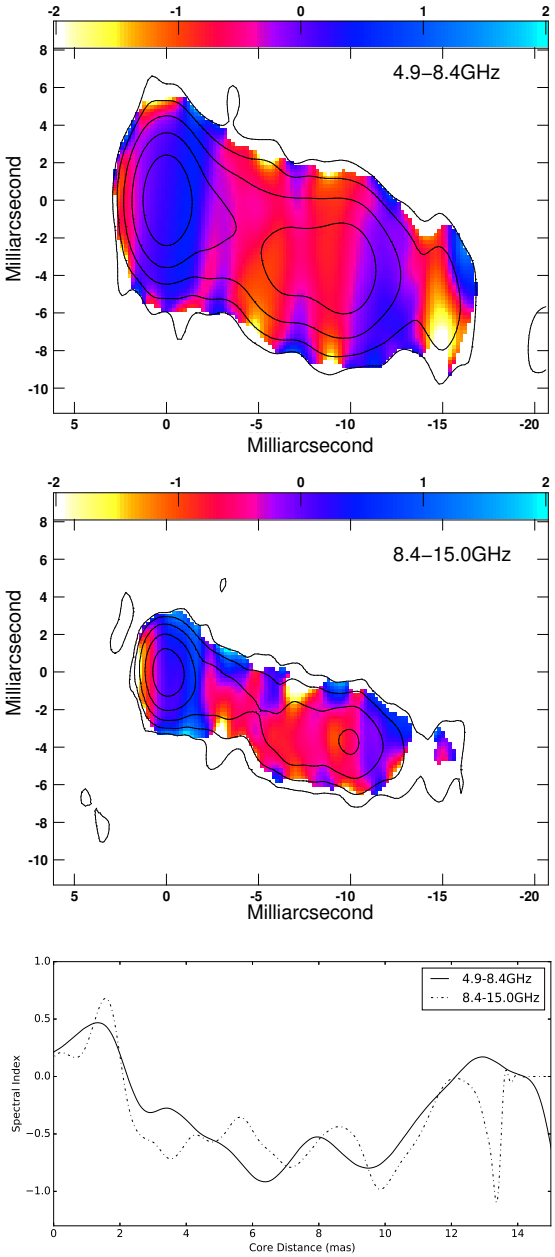

Fig. 3 The upper and middle panels show the distribution of the spectral index calculated between 4.9 and 8.4 GHz and between 8.4 and 15.0 GHz respectively. The spectral index maps are produced with the data of the VLBA track conducted in the epoch of 2002.55. The pseudo-color are superimposed on the contour plots of total intensity of 4.9 and 8.4 GHz respectively, in which the contours show $3\sigma\times(1, 4, 16, 64, 256, 1024)$. The color is shown where the intensity is above 3σ. The lower panel shows the spectral index along the jet axis as a function of the core distance.

and the region between 10–14 mas from the map center. Between these two regions, steep spectrum with $\alpha \sim -1$ is detected.

The lower panel of Figure 3 shows α along the approximate jet axis evolving with the distance from the core (we use the position of the 8.4 GHz VLBI core, and core-shifts between frequencies are ignored). Within 2.0 mas from the core, inverted spectrum with $\alpha > 0$ is detected, indicating that the emission from this region is very optical thick. Especially within 1.6 mas, the spectral index increases going outward, indicating that the opacity of the innermost jet is even higher than the VLBI core. Thus the free-free absorption (FFA) of the surrounding medium may attribute a lot to the high opacity as well as the synchrotron self-absorption (SSA) in the vicinity of the core. Beyond 2.0 mas, the spectrum goes steeper, i.e. the opacity de-

creases, as going outward. At 6–7 mas from the core, the spectral index reaches its minimum. Beyond the minimum, the spectral index increases as going outward, and the inverted spectrum appears again between 12 and 14 mas from the core.

3.3 Kinematics of the pc-scale Jet

With three epochs (1997.35, 2002.55, and 2010.51) of 8.4 GHz VLBA observations spanning 13 years, we obtain the proper motion of the pc-scale jet component A2, A3, A4 and A5. We fit their core distance increasing with time with a linear regression program, and use the inverse square of the uncertainty of the core distance as the weighting parameter in the fitting. Figure 4 presents their core distance measured from three epochs of 8.4 GHz VLBA data, overlapping with the fitting results of the proper motion.

The fitting proper motion for components A5, A4, A3 and A2 are 0.021±0.002, 0.038±0.001, 0.138±0.009, and 0.096±0.007 mas yr^{-1} respectively, corresponding to the apparent transverse velocities ($\beta_{\rm app}$) of 0.59 ± 0.06, 1.08 ± 0.03, 3.94 ± 0.26, and 2.72 ± 0.20 respectively in the unit of c. $\beta_{\rm app}$ increases from sub-luminal to superluminal between A5 and A3, and a mild deceleration follows in the region from A3 to A2.

As shown in Section 3.1, the average value of $T_{\rm b}$ of the VLBI core is about twice of the $T_{\rm eq}$, so it is proper to consider the Doppler factor $\delta \approx 2$. Then the bulk Lorentz factor γ, the viewing angle θ, and the intrinsic velocity β in the unit of c could be estimated as in Ghisellini et al. (1993).

$$\gamma = \frac{\beta_{\rm app}^2 + \delta^2 + 1}{2\delta}, \tag{3}$$

$$\theta = \arctan\ (\frac{2\beta_{\rm app}}{\beta_{\rm app}^2 + \delta^2 - 1}), \tag{4}$$

$$\beta = \frac{\beta_{\rm app}}{\sin\theta + \beta_{\rm app}\cos\theta}, \tag{5}$$

For A5, A4, A3 and A2, γ is estimated to be 1.3, 1.5, 3.1, and 5.1, respectively, β is 0.67, 0.76, 0.98 and 0.95, respectively, while θ is 19°, 27°, 23°, and 28°, respectively.

3.4 Polarization of the pc-scale Jet

We successfully made polarimetry on PKS 1229−02 at 1.6 GHz in the epoch of 2000.15 and at 4.9 and 8.4 GHz in the epoch of 2002.55. The results are shown in Figure 5, in which the fractional polarization (F_p) is presented in pseudo-color superimposed on the contour plots of total intensity, and the vectors represent the observed EVPA. The color is only shown where the polarized intensity is above 3σ.

As Figure 5 shows, at 1.6 GHz, the core region is weakly polarized with $F_p < 1\%$, while the jet within 10 mas from the core is polarized with $F_p < 6\%$ and the EVPA is roughly parallel to the direction of the jet. At 4.9 GHz, the polarized emission is detected along the jet between 2 and 14 mas from the core; the highest value of F_p (40%) appears at the edge of the jet, which is about 6 mas from the core. The EVPA is roughly parallel to the jet between 2 and 3 mas from the core, while for the rest region, the EVPA is almost perpendicular to the jet. At 8.4 GHz, the configuration of the polarized emission is quite similar with that of 4.9 GHz. The polarized emission starts to be detected at only 1 mas from the core, and the peak value of the F_p is even larger ($\sim 60\%$).

At 1.6 GHz, the core region is weakly polarized, while at 4.9 and 8.4 GHz it is not polarized at all. This is possibly due to the lower angular resolution at 1.6 GHz, thus the observed core is a mixture of the real core and the innermost jet.

4 DISCUSSION

4.1 Interaction between the Jet and the Ambient Medium

As we have mentioned in Section 3.3, between the jet component A5 and A3, the apparent transverse velocity of the pc-scale jet increases from sub-luminal to superluminal. Acceleration observed in pc-scale jets in AGNs is usually interpreted as a consequence of the azimuthal magnetic field pressure gradient in the jet (Vlahakis & Königl 2004). For PKS 1229−021, the acceleration seems very efficient, but magnetic field may not be the only factor affecting the bulk motion of its pc-scale jet.

We mark the locations of the pc-scale jet components on the figure showing the spectral index α evolving with the distance from the core (see the upper panel of Fig. 6), and find that there is a clear relation between the apparent transverse velocity and the opacity of the pc-scale jet in PKS 1229−021: the apparent transverse velocity increases as the opacity decreases. Moreover, the acceleration rate is not a constant, e.g. the acceleration rate is $0.21c$ mas^{-1} from A5 to A4, much lower than that from A4 to A3, which is as high as $0.61c$ mas^{-1}. As we have mentioned in Section 3.2, significant absorption features are found between A5 and A4, indicating the surrounding medium might be very dense in this region, thus the interaction between the jet and medium may counteract a

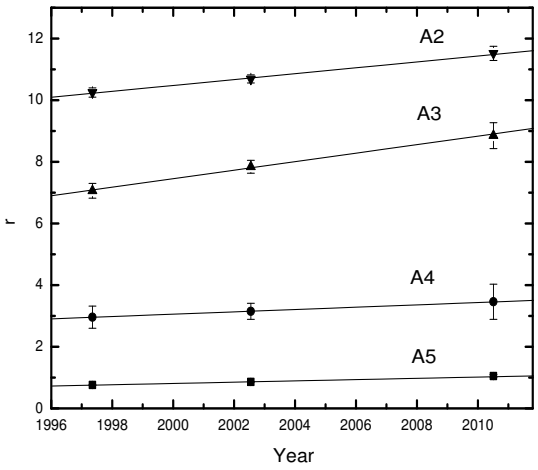

Fig. 4 Core distance of the pc-scale jet components A5, A4, A3, and A2 in three epochs (1997.35, 2002.55, and 2010.51) measured with 8.4 GHz VLBA data, overlapping with the fitting results of their proper motion.

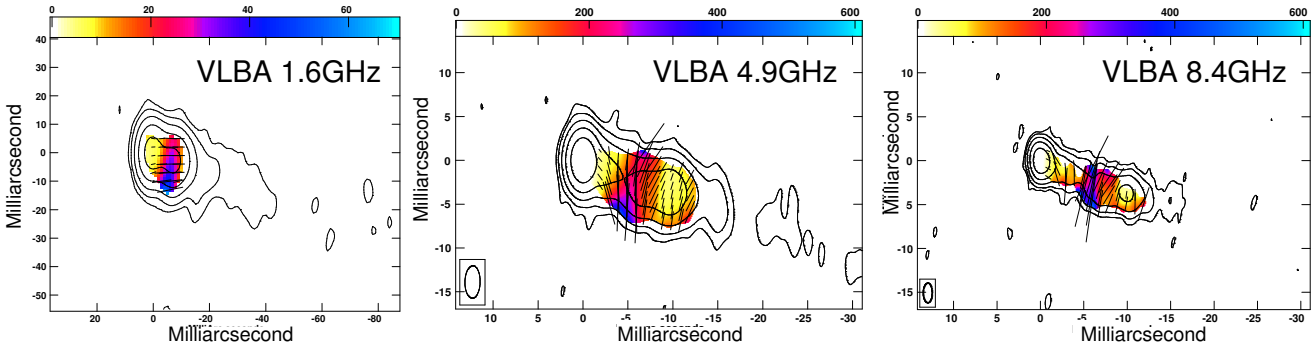

Fig. 5 Results of polarimetry of PKS 1229−02 at 1.6 GHz in the epoch of 2000.15, and at 4.9 GHz and 8.4 GHz in the epoch of 2002.55. The pseudo-color presents the fractional polarization F_p, and the unit used in the color-scale is Milli-percentage. The vectors presents the EVPA. The pseudo-color and vectors are superimposed on the contour plots of total intensity, in which the contours show $3\sigma\times(1, 4, 16, 64, 256)$.

large part of the magnetic-driving acceleration. From A4 to A3, the opacity decreases significantly, thus jet-medium interaction may get weaker in this region, so the magnetic-driving acceleration becomes much more efficient and this is why the acceleration rate is much higher in this region than that between A5 and A4.

A mild deceleration is found from A3 to A2, corresponding to the increase of the opacity in the region, suggesting that the jet-medium interaction may have counteracted the acceleration completely. In addition, the jet is found brightened around A2, i.e. the integral flux density of the component A2 is higher than that of A3 and A4 in any epoch at any frequency. So, we infer that a shock is probably formed in this region, then the emitting particles are re-accelerated and the local magnetic field is enhanced. A part of the kinetic energy of the bulk motion is transferred to the radiant energy by the shock, thus the bulk motion slows down and the jet is brightened in this region. Another possible consequence of the enhancement of the local magnetic field is the increasing of the SSA opacity, so SSA may contribute a lot to the large opacity beyond A2, as well as the FFA.

The lower panel of Figure 6 shows the factional polarization F_p along the jet axis measured at 4.9 and 8.4 GHz (see Sect. 3.4) as a function of the core distance. Comparing with the upper panel, it is clearly seen that F_p increases as the opacity decreases. The F_p peaks between 6 and 7 mas from the core, just where the opacity approaches to its minimum. Beyond the peak, the F_p decreases as the opacity increases until 10 mas from the core. It reminds us that, the surrounding medium might have significantly depolarized the emission. Beyond 10 mas from the core,

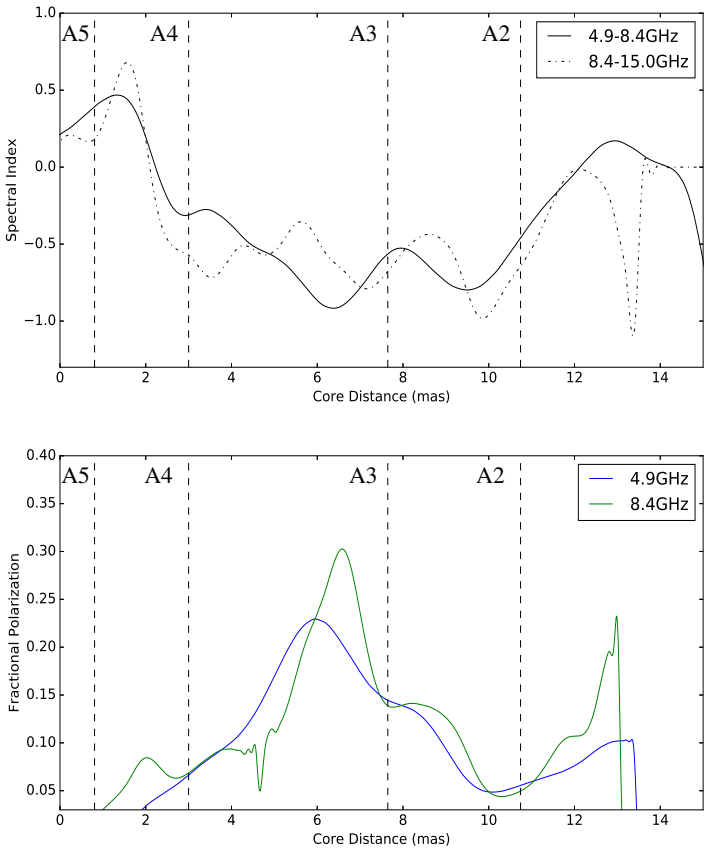

Fig. 6 The upper panel shows the spectral index evolving with the core distance as in Fig. 3, marked with fitted locations of the pc-scale jet components. The lower panel shows the fractional polarization F_p evolving with the core distance, which is obtained from the polarimetry at 4.9 GHz and 8.4 GHz in the epoch of 2002.55 shown in Fig. 5.

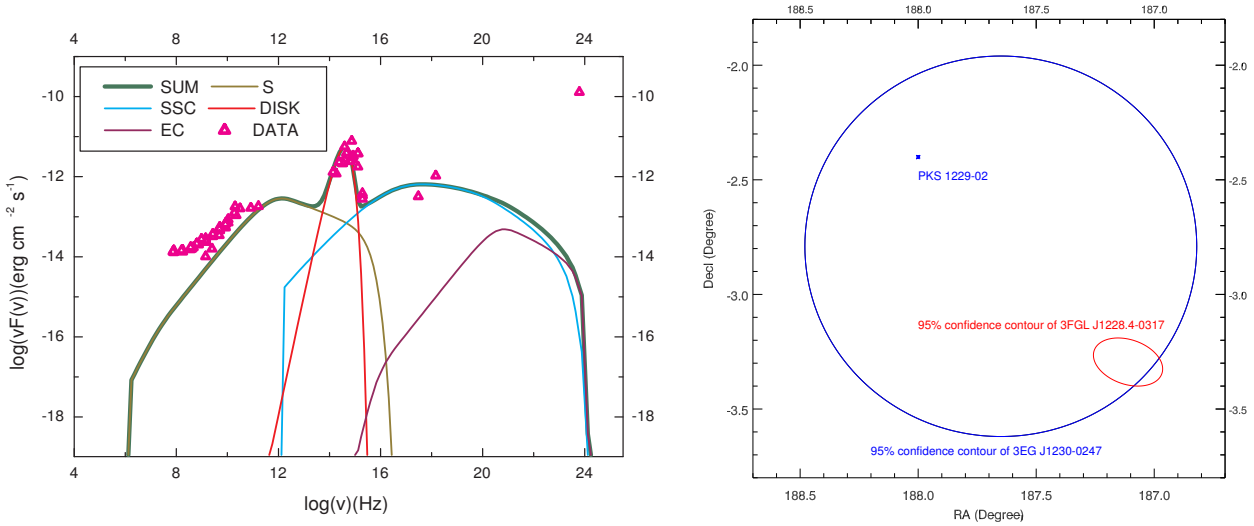

Fig. 7 The left panel shows the data of flux density of PKS 1229–02 obtained from NED (DATA), overlapping with the best-fitting SED (SUM) using a model including synchrotron processes (S), self-Inverse Compton processes (SSC), outer-Inverse Compton processes (EC), and thermal emission from the accretion disk (DISK). The right panel shows the positions of PKS 1229–02, 3EG J1230–0247, and 3FGL J1228.4–0317 on the sky plane. The blue circle represents the 95% confidence region of 3EG J1230–0247, the blue asterisk marks the optical position of PKS 1229−02, and the red elliptic presents the 95% confidence region of 3FGL J1228.4–0317.

F_p increases as the opacity increases as going outward, indicating that the shock formed around A2 might have enhanced the polarization and the SSA opacity at the same time. The surrounding medium may have also brought significant rotation of the EVPA, since for the region with high opacity, e.g. as Figure 5 shows, at 4.9 and 8.4 GHz, in the innermost part of the jet, the EVPA is parallel to jet, while for the outer region with lower opacity, the EVPA is perpendicular to the jet.

We conclude that the anterograde jet of PKS 1229−02 is surrounded by nonuniform dense ambient medium, while the retrograde jet is not. From the first few parsecs, to tens of kilo-parsecs away from its base, the anterograde jet always interacts intensively with the surrounding medium. The collisions between the jet and the medium have even evoked shocks, building the knotty morphology of the anterograde jet from pc to kpc-scale. The shocks have transferred a part of the kinetic energy of the jet to the radiant energy, and this is why the anterograde jet is brighter but more stubby than its retrograde counterpart in kpc-scale.

4.2 Misidentification as a γ-ray AGN

As our observing results show, PKS 1229−02 is not compact on both kpc and pc-scales, while the $T_{\rm b}$ of its VLBI core is as the same order of magnitude as the $T_{\rm eq}$. It shows a very low variability in the radio band as in the optical band, e.g. for all epochs of VLBI observations spanning 13 years in this paper, the total integral flux density of this source varies between a narrow range from 572 to 729 mJy. So we conclude that, in PKS 1229−02, the effects of relativistic time dilation, Doppler boosting, or projection are not prominent.

Based on the results of our observations, we reproduce the SED of PKS 1229−02. It was once produced by Chiappetti et al. (2004) and Tavecchio et al. (2007) using δ between 10 and 14, which is much larger than our estimated value ($\delta \approx 2$). We use a model including synchrotron processes, self-Inverse Compton processes, outer-Inverse Compton processes, and thermal emission from the accretion disk. The details of the model are described in Massaro et al. (2006); Tramacere et al. (2009, 2011), the numerical code of the model is developed by Andrea Tramacere. For parameters such as magnetic field, size of the jet, temperature of the accretion disk, luminosity of the BLR, we use the same values as used in Tavecchio et al. (2007). For the the Bulk Lorentz factor (γ) and the viewing angle (θ) of the jet, based on the estimated value of pc-scale jet shown in Section 3.3, we adjust γ between 1 and 6, while θ between 15° and 30° respectively to fit our model to the historical data obtained from NASA/IPAC Extragalactic Database (NED) [2].

We find that if we exclude the γ-ray data, our model fits the rest of the data best when $\gamma = 4$ and $\theta = 18°$ (i.e. $\delta = 1.6$). The left panel of Figure 7 presents the NED data overlapping with the best-fitting model. But, no matter how we adjust γ and θ, the prospected flux density in the γ-ray band is much lower than the NED value given by Thompson et al. (1995); Hartman et al. (1999). This result suggests that in PKS 1229−02 the relativistic beaming effect might not be strong enough to produce the reported γ-ray emission. Although a small number of γ-ray sources are identified as AGNs without strong beaming effect, e.g. the radio galaxies M87, the compact steep-spectrum source 4C+39.23B, or the narrow-line Seyfert 1 galaxy PKS 2004–447, PKS 1229−02 shows very little similarities with these sources. Also we have compared the positions of PKS 1229−02, 3EG J1230–0247 and 3FGL J1228.4–0317 on the sky plane. As the right panel of Figure 7 shows, the optical position of PKS 1229−02 in Sloan Digital Sky Survey is right within the 95% confidence region of 3EG J1230–024, but out of the 95% confidence region of 3FGL J1228.4–0317, and the distance from the quasar to the center of the confidence region is as far as 1.5°. So PKS 1229−02 may probably could not produce any detectable γ-ray emission. It was misidentified as the radio and optical counterpart of a γ-ray source, due to the poor resolution of the detector of EGRET.

Acknowledgements The VLBA is an instrument of the National Radio Astronomy Observatory. The National Radio Astronomy Observatory is a facility of the National Science Foundation operated under cooperative agreement by Associated Universities, Inc. The European VLBI Network is a joint facility of European, Chinese, South African and other radio astronomy institutes funded by their national research councils.

References

Abdo, A. A., Ackermann, M., Ajello, M., et al. 2009, ApJS, 183, 46

Arbeiter, C., Pohl, M., & Schlickeiser, R. 2002, A&A, 386, 415

Bloom, S. D., & Marscher, A. P. 1996, ApJ, 461, 657

Böttcher, M. 2000, in American Institute of Physics Conference Series, 515, eds. B. L. Dingus, M. H. Salamon, & D. B. Kieda, 31

[2] http://ned.ipac.caltech.edu/

Chiappetti, L., Ghisellini, G., Maraschi, L., et al. 2004, Nuclear Physics B Proceedings Supplements, 132, 161
Dermer, C. D., & Schlickeiser, R. 1993, ApJ, 416, 458
Diamond, P. J. 1995, in Astronomical Society of the Pacific Conference Series, 82, Very Long Baseline Interferometry and the VLBA, eds. J. A. Zensus, P. J. Diamond, & P. J. Napier, 227
Dondi, L., & Ghisellini, G. 1995, MNRAS, 273, 583
Fomalont, E. 2004, Error Recognition and Image Analysis, Ninth Synthesis Imaging Summer School Socorro, June 15–22, *http://www.aoc.nrao.edu/events/synthesis/2004/presentations/FomalontErrorRecognition.pdf*
Ghisellini, G., Padovani, P., Celotti, A., & Maraschi, L. 1993, ApJ, 407, 65
Guijosa, A., & Daly, R. A. 1996, ApJ, 461, 600
Hartman, R. C., Bertsch, D. L., Bloom, S. D., et al. 1999, ApJS, 123, 79
Kronberg, P. P., Perry, J. J., & Zukowski, E. L. H. 1992, ApJ, 387, 528
Le Brun, V., Bergeron, J., Boisse, P., et al. 1997, A&A, 321, 733
Lee, S.-S., Lobanov, A. P., Krichbaum, T. P., et al. 2008, AJ, 136, 159
Maraschi, L., Ghisellini, G., & Celotti, A. 1992, ApJ, 397, L5
Marscher, A. P., & Gear, W. K. 1985, ApJ, 298, 114
Massaro, E., Tramacere, A., Perri, M., et al. 2006, A&A, 448, 861
Mücke, A., & Protheroe, R. J. 2001, Astroparticle Physics, 15, 121
Protheroe, R. J. 1997, in Astronomical Society of the Pacific Conference Series, 121, IAU Colloq. 163: Accretion Phenomena and Related Outflows, eds. D. T. Wickramasinghe, G. V. Bicknell, & L. Ferrario, 585
Rachen, J. P. 2000, in American Institute of Physics Conference Series, 515, eds. B. L. Dingus, M. H. Salamon, & D. B. Kieda, 41
Raiteri, C. M., Ghisellini, G., Villata, M., et al. 1998, A&AS, 127, 445
Readhead, A. C. S. 1994, ApJ, 426, 51
Romero, G. E., Cellone, S. A., Combi, J. A., et al. 2002, A&A, 390, 431
Shepherd, M. C., Pearson, T. J., & Taylor, G. B. 1994, in BAAS, Vol. 26, Bulletin of the American Astronomical Society, 987
Tavecchio, F., Maraschi, L., Wolter, A., et al. 2007, ApJ, 662, 900
Thompson, D. J., Bertsch, D. L., Dingus, B. L., et al. 1995, ApJS, 101, 259
Tramacere, A., Giommi, P., Perri, M., Verrecchia, F., & Tosti, G. 2009, A&A, 501, 879
Tramacere, A., Massaro, E., & Taylor, A. M. 2011, ApJ, 739, 66
Vlahakis, N., & Königl, A. 2004, ApJ, 605, 656
Wills, B. J., Wills, D., Breger, M., Antonucci, R. R. J., & Barvainis, R. 1992, ApJ, 398, 454
Wright, E. L. 2006, PASP, 118, 1711